Room-temperature ferrimagnetism of anti-site-disordered Ca_2MnOsO_6

Hai L. Feng (冯海),[1,2,3,*,†] Madhav Prasad Ghimire,[4,5,6] Zhiwei Hu,[2] Sheng-Chieh Liao,[2] Stefano Agrestini,[2,7] Jie Chen,[1,8] Yahua Yuan,[1,9] Yoshitaka Matsushita,[10] Yoshihiro Tsujimoto,[1,8] Yoshio Katsuya,[11] Masahiko Tanaka,[11] Hong-Ji Lin,[12] Chien-Te Chen,[12] Shih-Chang Weng,[12] Manuel Valvidares,[7] Kai Chen,[13] Francois Baudelet,[13] Arata Tanaka,[14] Martha Greenblatt,[3] Liu Hao Tjeng,[2] and Kazunari Yamaura[1,8,*]

[1]*Research Center for Functional Material, National Institute for Materials Science, 1-1 Namiki, Tsukuba, Ibaraki 305-0044, Japan*
[2]*Max Planck Institute for Chemical Physics of Solids, Nöthnitzer Str. 40, 01187 Dresden, Germany*
[3]*Department of Chemistry and Chemical Biology, Rutgers, the State University of New Jersey, 610 Taylor Road, Piscataway, New Jersey 08854, USA*
[4]*Central Department of Physics, Tribhuvan University, Kirtipur, 44613 Kathmandu, Nepal*
[5]*Leibniz Institute for Solid State and Materials Research, IFW Dresden, P.O. Box 270116, D-01171 Dresden, Germany*
[6]*Condensed Matter Physics Research Center, Butwal-11, Rupandehi, Nepal*
[7]*ALBA Synchrotron Light Source, E-08290 Cerdanyola del Vallès, Barcelona, Spain*
[8]*Graduate School of Chemical Sciences and Engineering, Hokkaido University, North 10 West 8, Kita-ku, Sapporo, Hokkaido 060–0810, Japan*
[9]*School of Physics and Electronics, Central South University, Changsha 410083, China*
[10]*Materials Analysis Station, National Institute for Materials Science, 1-2-1 Sengen, Tsukuba, Ibaraki 305-0047, Japan*
[11]*Synchrotron x-ray Station at SPring-8, National Institute for Materials Science, Kouto 1-1-1, Sayo-cho, Hyogo 679–5148, Japan*
[12]*National Synchrotron Radiation Research Center, 101 Hsin-Ann Road, Hsinchu 30076, Taiwan, ROC*
[13]*Synchrotron SOLEIL, L'Orme des Merisiers, Saint-Aubin, 91192 Gif-sur-Yvette Cedex, France*
[14]*Department of Quantum Matter, ADSM, Hiroshima University, Higashi-Hiroshima 739–8526, Japan*

(Received 7 August 2019; published 16 December 2019)

Room-temperature ferrimagnetism was discovered for the anti-site-disordered perovskite Ca_2MnOsO_6 with $T_c = 305$ K. Ca_2MnOsO_6 crystallizes into an orthorhombic structure with a space group of *Pnma*, in which Mn and Os share the oxygen-coordinated-octahedral site at an equal ratio without a noticeable ordered arrangement. The material is electrically semiconducting with variable-range-hopping behavior. X-ray absorption spectroscopy confirmed the trivalent state of the Mn and the pentavalent state of the Os. X-ray magnetic circular dichroism spectroscopy reveals that the Mn and Os magnetic moments are aligned antiferromagnetically, thereby classifying the material as a ferrimagnet which is in accordance with band structure calculations. It is intriguing that the magnetic signal of the Os is very weak, and that the observed total magnetic moment is primarily due to the Mn. The $T_c = 305$ K is the second highest in the material category of so-called disordered ferromagnets such as $CaRu_{1-x}Mn_xO_3$, $SrRu_{1-x}Cr_xO_3$, and $CaIr_{1-x}Mn_xO_3$, and hence, may support the development of spintronic oxides with relaxed requirements concerning the anti-site disorder of the magnetic ions.

DOI: 10.1103/PhysRevMaterials.3.124404

I. INTRODUCTION

Double perovskite oxides containing 3*d* and 4*d*/5*d* elements are currently much in focus since promising properties for spintronic applications have been reported. For example, Sr_2FeMoO_6 shows a low-field magnetoresistance at room temperature [1], and Sr_2CrReO_6 half-metallic (HM) transport with a remarkably high Curie temperature (T_c) of 635 K [2,3]. Analogous closely related ferrimagnetic (FIM) oxides have been synthesized with a wide variety of 3*d* and 4*d*/5*d* elements, such as A_2FeMoO_6 (A = Ca, Ba) [1,4], A_2FeReO_6 (A = Ca, Sr, Ba) [5,6], Ca_2CrOsO_6 [2,3], and Ca_2FeOsO_6 [7,8]. In addition, a ferromagnetic (FM) Dirac–Mott insulating state ($T_c \sim 100$ K) has been found in Ba_2NiOsO_6 [9] and an exchange bias effect in $Ba_2Fe_{1.12}Os_{0.88}O_6$ [10], which may also be useful for further development of spintronic oxides.

In the magnetic ground state of Sr_2FeMoO_6 and Sr_2CrReO_6, the 3*d* magnetic moments are ordered parallel to each other and antiparallel to those of the 4*d*/5*d* [1–3]. Anti-site disorder between the 3*d* and 4*d*/5*d* elements has, however, a significant negative impact on the magnetic properties, because strongly antiferromagnetic (AFM) Fe–O–Fe and Cr–O–Cr bonds are formed that interfere with the long-range magnetic order [11,12]. Indeed, even a small degree of anti-site disorder dramatically decreases T_c, and the spin polarization is also strongly reduced in Sr_2FeMoO_6 [13,14], accompanied by a linearly decreasing saturation magnetization [12]. Therefore, accurate control of the anti-site disorder has been a significant issue for the fabrication of practical devices since growing anti-site-disorder-free materials is

*Corresponding authors hai.feng@iphy.ac.cn, hai.feng_nims@hotmail.com; yamaura.kazunari@nims.go.jp
†Present address: The Institute of Physics, Chinese Academy of Sciences, P.O. Box 603, Beijing 100190, China.

highly challenging [11,12]. Alternatively, anti-site-disorder tolerant materials with promising properties are in demand.

A so-called disordered FM has been reported in a substitutional study of the paramagnetic perovskite $CaRuO_3$, where Ru is partially replaced by a variety of magnetic or nonmagnetic elements such as Sn, Ti, Mn, Fe, Ni, or Rh [15,16]. Among these, Ca_2MnRuO_6 is particularly of high interest, because its magnetic moment is relatively large ($\sim 1.6\,\mu_B$/f.u.) and its T_c is high ($\sim$230 K) [17,18]. In the structure of Ca_2MnRuO_6, Mn and Ru are distributed over the perovskite *B* site at an equal ratio without an ordered arrangement. This material was revealed to be FIM by neutron diffraction owing to a balance between FM (Mn^{3+} to Mn^{4+}) and AFM (Ru to Mn) interactions [17–19], and the experimental magnetic state was consistent with that obtained by first-principles calculations [19]. Another example is $SrRu_{0.6}Cr_{0.4}O_3$ which was found to have a high transition temperature of 400 K but a very small saturated moment of 0.15 μ_B/f.u. [20].

In this study, an anti-site-disordered compound, Ca_2MnOsO_6 was synthesized by a high-pressure and high-temperature method at 6 GP and 1500 °C. Ca_2MnOsO_6 shows a FIM transition at $T_c = 305$ K, which is the second highest T_c among the disordered FMs. Here we report the refined crystal structure and bulk magnetic properties of Ca_2MnOsO_6. The results suggest that the compound is useful for further development of anti-site-disorder-tolerant spintronic oxides.

II. EXPERIMENTAL

Polycrystalline Ca_2MnOsO_6 was synthesized via a solid-state reaction from powders of CaO_2 (lab-made from $CaCl_2 \cdot 2H_2O$, 99% Wako Pure Chem.), Os (99.95%, Heraeus Materials), and MnO_2 (99.997%, Alfa-Aesar). The powders were thoroughly mixed at the stoichiometric ratio, followed by sealing in a Pt capsule. The preparation was conducted in an Ar-filled glove box. The Pt capsule was statically and isotropically compressed in a belt-type high-pressure apparatus (Kobe Steel, Ltd., Japan [21]), and a pressure of 6 GPa was continuously applied while the capsule was heated at 1500 °C for 1 h, followed by quenching to room temperature in less than a minute. The pressure was then gradually released over several hours.

A dense, black polycrystalline pellet was obtained, and several pieces were cut out from it. A selected piece was finely ground for a synchrotron x-ray diffraction (SXRD) study, which was conducted in a large Debye-Scherrer camera in the BL15XU beam line, SPring-8, Japan [22,23]. The SXRD pattern was collected at room temperature and the wavelength was confirmed to be 0.65298 Å by measurement of a standard material, CeO_2. The absorption coefficient was measured in the same line. The Rietveld method was used to analyze the SXRD pattern with the RIETAN-VENUS software [24,25].

X-ray absorption spectroscopy (XAS) at the Mn-$L_{2,3}$ and Os-L_3 edges of Ca_2MnOsO_6 was carried out at the BL11A and BL07C beamlines using the total electron yield and transmission method, respectively, in the National Synchrotron Radiation Research Center, Taiwan. The Mn-$L_{2,3}$ spectrum of MnO and the Os-L_3 spectrum of Sr_2FeOsO_6 were also measured for energy calibration purposes. X-ray magnetic circular dichroism (XMCD) spectra at the Mn-$L_{2,3}$ and the Os-$L_{2,3}$ edges were obtained at the BL29 BOREAS beamline of the ALBA synchrotron radiation facility in Barcelona and at the ODE beamline of Soleil France, respectively. The degree of circular polarization in BOREAS and ODE beamline was close to 100% and 90%, respectively. The XMCD spectra were measured in a magnetic field of 60 kOe at a temperature of 20 K for Mn-$L_{2,3}$ and in 13 kOe at 4 K for the Os-$L_{2,3}$. The Os L_3/L_2 edge-jump intensity ratio $I(L_3)/I(L_2)$ was normalized to 2.08 [26], which accounts for the difference in the radial matrix elements of the $2p_{1/2} -$ to $- 5d(L_2)$ and $2p_{3/2} -$ to $- 5d(L_3)$ transitions.

The electrical resistivity (ρ) of polycrystalline Ca_2MnOsO_6 was measured by a four-point method at a gauge current of 0.1 mA in a physical properties measurement system (Quantum Design, Inc.). Electrical contacts on a piece of Ca_2MnOsO_6 were prepared using Pt wires and Ag paste in the longitudinal direction. The temperature dependence of the specific heat capacity (C_p) was measured in the same apparatus by a thermal relaxation method at temperatures between 2 and 300 K using Apiezon N grease to thermally connect the material to the holder stage.

The magnetic susceptibility (χ) of a loosely gathered Ca_2MnOsO_6 powder was measured in a magnetic properties measurement system (Quantum Design, Inc.). The measurement was conducted in field cooling (FC) and zero-field cooling (ZFC) conditions in a temperature range between 2 and 390 K. The applied magnetic field was 10 kOe. The magnetic field dependence of the magnetization (M) was measured between -50 and $+50$ kOe at fixed temperatures of 2, 200, 300, and 350 K. The alternative current (ac) χ was measured in the same apparatus between 5 and 320 K; the amplitude and frequencies of the ac-magnetic field were 5 Oe and 0.5–500 Hz, respectively.

The density functional theory (DFT) calculation was performed on Ca_2MnOsO_6 with the all-electron full-potential local-orbital code [27] using the standard generalized-gradient approximation (GGA) [28]. In this study, a linear tetrahedron method was employed for all k space integration with a $12 \times 12 \times 12$ subdivision in the full Brillouin zone for an ordered phase of Ca_2MnOsO_6. The magnetic ground state was obtained by computing the total energy of possible magnetic configurations. Our calculation was double-checked in selected cases using the full-potential linearized augmented plane wave method, as implemented in the WIEN2K code [29]. In order to estimate the correlation effects, the GGA+U (U is the Coulomb interaction) function with atomic-limit double-counting correction was used [30,31]. The values of U were chosen to be 5 eV for Mn-3d and 1.5 eV for Os-5d, which were comparable to the values in the literature [9,32–36]. The self-consistent full-relativistic calculations were carried out with spin-orbit coupling (SOC) included. This is necessary to determine the magnetic anisotropy energy (MAE) and to check its influence on the electronic and magnetic properties. The calculation was first performed with the experimental lattice parameters obtained by SXRD, and then geometry optimization was conducted. The energy and charge convergence for the self-consistent calculation was set to 10^{-8} Hartree and 10^{-6} of electron, respectively.

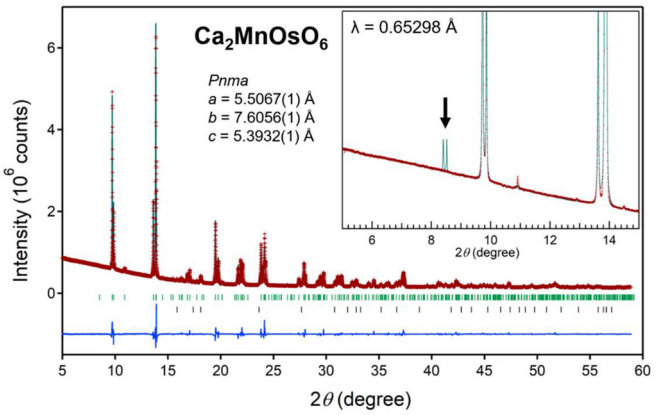

FIG. 1. Rietveld refinement of the powder synchrotron XRD pattern collected at room temperature. The crosses and solid lines show the observed and calculated patterns, respectively, with their difference shown at the bottom. The Os was analyzed simultaneously as the secondary phase. The estimated mass proportion was Ca_2MnOsO_6. Os = 0.986. 0.014. (Inset) Analysis by an ordered Mn and Os atoms model; the arrow indicates an obvious discrepancy between the model and the experiment in the analysis.

III. RESULTS

A. Crystal structure

The double perovskite oxide $A_2BB'O_6$ [A: alkali earth, B : $3d$, B' : $4d(5d)$ elements] normally crystallizes into a monoclinic ($P2_1/n$), or tetragonal ($I4/m$), or cubic (Fm-$3m$) structure, in which two distinct octahedra BO_6 and $B'O_6$ align in a rocksalt fashion [37]. The degrees of the octahedral distortion and rotation seem to have a major impact on the lattice symmetry [38]. Based on the general trend, we attempted to characterize the crystal structure of Ca_2MnOsO_6 by applying these models. In particular, the monoclinic model ($P2_1/n$) was very effective to refine the SXRD pattern as reported for the analogous compounds such as Ca_2FeOsO_6 [7], Ca_2CrOsO_6 [2], and Ca_2MnReO_6 [39]. The refinement quality was, however, not fully satisfactory: a significant failure was found for the peaks marked by an arrow in the inset of Fig. 1. Although the major peaks were well refined by the $P2_1/n$ model (if Mn and Os are fully ordered), several expected peaks such as (0−11), (−101), and (101) were not observed above the background level. This failure suggested that the rocksalt-type ordered arrangement of MnO_6 and OsO_6 octahedra is not formed in Ca_2MnOsO_6 [13], namely, Os and Mn atoms are distributed randomly over the perovskite B site (i.e., anti-site disorder), as was found in Ca_2MnRuO_6 (*Pnma* [17]).

We therefore tested the *Pnma* model of the SXRD data, and as shown in the main panel of Fig. 1, the *Pnma* model successfully characterized the structure of Ca_2MnOsO_6. The final solutions of the lattice parameters, atomic coordinates, and temperature factors are listed in Table I. Note that the orthorhombic model (*Pnma*) was proposed for both end compounds, $CaOsO_3$ [40] and $CaMnO_3$ [41] as well, which indicates that Ca_2MnOsO_6 is not a double perovskite, but a solid solution of them.

The average of the M-O (M = Mn or Os) bond lengths of Ca_2MnOsO_6 is compared with that of related compounds;

TABLE I. Atomic coordinates and temperature factors (B) for Ca_2MnOsO_6 at room temperature obtained from synchrotron XRD. Space group. *Pnma*; lattice constants $a = 5.50669(4)$ Å, $b = 7.60567(6)$ Å, and $c = 5.39322(4)$ Å; $Z = 2$; $d_{cal} = 6.1946$ g/cm^3; and the final R indices are $R_p = 2.029\%$ and $R_{wp} = 3.597\%$.

Atom	Site	Occp.	x	y	z	B(Å^2)
Ca	4c	1	0.9523(3)	0.25	0.0102(9)	1.12(3)
Os/Mn	4b	0.5/0.5	0	0	0.5	0.22(1)
O1	4c	1	0.0340(11)	0.25	0.5718(10)	1.03(8)
O2	8d	1	0.2106(7)	0.4578(5)	0.1850(7)	1.03

it is shorter than that of $CaOs^{4+}O_3$ [40] and $LaMn^{3+}O_3$ [42] and longer than that of $NaOs^{5+}O_3$ [43] and $CaMn^{4+}O_3$ [41] (see Table II). The comparison suggests that the valence state of M is intermediate between the two groups. In addition, we examined the impact of the Jahn-Teller (JT) distortion on the average structure through comparison of the distortion factors (defined as the ratio of the longest to the shortest M–O length of an octahedron) of the compounds. It is 1.084 for Ca_2MnOsO_6, which is much smaller than 1.142 for $LaMn^{3+}O_3$ and much greater than 1.004 for $CaMn^{4+}O_3$, 1.030 for $CaOs^{4+}O_3$, and 1.004 for $NaOs^{5+}O_3$. Although the comparison indicates that the JT distortion could contribute to the average structure of Ca_2MnOsO_6, it is extremely difficult to uniquely identify the exact charge distribution on Mn and Os of Ca_2MnOsO_6 from only an analysis of the powder SXRD pattern, because of the anti-site disorder.

B. X-ray absorption spectroscopy

To investigate the valence states of Mn and Os, we conducted the Mn-$L_{2,3}$ and Os-L_3 XAS on Ca_2MnOsO_6 and compared the spectra to those of MnO [44], $LaMnO_3$ [44], $SrMnO_3$ [45], and Sr_2FeOsO_6 [46] which serve as Mn^{2+}, Mn^{3+}, and Mn^{4+}, and Os^{5+} references, respectively (see Fig. 2). The spectral weight of the L_3 white line shifts to higher energies by 1 eV or more as the Mn valence state increases by one: from Mn^{2+} (MnO) to Mn^{3+} ($LaMnO_3$) and further to Mn^{4+}($SrMnO_3$) [44,45]. The similar energy position and multiplet spectral features of the Mn-$L_{2,3}$ of Ca_2MnOsO_6 and $LaMnO_3$ demonstrate the trivalent state of Mn in Ca_2MnOsO_6. Analogously, the Os-L_3 spectrum of Ca_2MnOsO_6 locates at the same energy as that of Ca_2FeOsO_6, indicating the pentavalent state of the Os [7,47], thereby fulfilling the charge balance requirement for the Mn^{3+}/Os^{5+} state. Consequently, the valence state of Ca_2MnOsO_6 (Mn^{3+}, Os^{5+}) is different from that of the analogous compound Ca_2MnRuO_6, in which the mixed valent states of (Mn^{3+}, Ru^{5+}) and (Mn^{4+}, Ru^{4+}) are degenerate in energy [17].

C. Electrical transport

Figure 3 shows an increasing resistivity $\rho(T)$ of Ca_2MnOsO_6 with lowering the temperature, experimentally demonstrating a semiconducting-like behavior. Interestingly, it is qualitatively and quantitatively different from the half-metallic behavior observed for the related compound Ca_2MnRuO_6 [17,19]. The temperature dependence of $\rho(T)$ is

TABLE II. Comparison of structural parameters of Ca_2MnOsO_6 and related compounds.

	$LaMn^{3+}O_3$ [42]	$CaMn^{4+}O_3$ [41]	Ca_2MnOsO_6 [this work]	$CaOs^{4+}O_3$ [40]	$NaOs^{5+}O_3$ [43]
Space group	*Pnma*	*Pnma*	*Pnma*	*Pnma*	*Pnma*
a (Å)	5.5367(1)	5.279(1)	5.50666(4)	5.57439(3)	5.38420(1)
b (Å)	5.7473(1)	7.448(1)	7.60562(6)	7.77067(4)	7.58038(1)
c (Å)	7.6929(2)	5.264(1)	5.39317(4)	5.44525(3)	5.32817(1)
V (Å^3)	244.8	207.0	225.9	235.9	217.5
M–O1 (Å)	1.9680(3) × 2	1.895 × 2	1.945(1) × 2	2.003(1) × 2	1.946(1) × 2
M–O2 (Å)	1.907(1) × 2	1.900 × 2	1.917(4) × 2	1.978(4) × 2	1.939(3) × 2
M–O2 (Å)	2.178(1) × 2	1.903 × 2	2.077(4) × 2	2.037(4) × 2	1.940(3) × 2
Distortion[a]	1.142	1.004	1.084	1.030	1.004
⟨*M*–O⟩ (Å)	2.018	1.899	1.980	2.006	1.942
M–O1–*M* (°)	155.48(2)	158.6	149.6(2)	151.7(1)	153.9(2)
M–O2–*M* (°)	155.11(5)	157.2	155.7(1)	152.0(2)	155.2(2)

[a]Defined as the ratio of the longest to the shortest *M*–O length of the MO_6 octahedron.

poorly characterized by the Arrhenius model at low temperatures (<300 K, inset of Fig. 3); however, a variable-range-hopping conduction model better explains the data (inset of Fig. 3) [48]. Although the Arrhenius model does not exactly fit the data, we can roughly estimate the lower limit of the thermal activation energy in the high-temperature region (>300 K) as ∼0.11 eV from the linear fit as shown in the inset of Fig. 3.

D. Magnetic properties

The magnetic susceptibility $\chi(T)$ curves measured in the ZFC and FC conditions for Ca_2MnOsO_6 are shown in Fig. 4. Upon cooling, there is an increasing value of χ at around 305 K, indicating the establishment of a FM-like transition. The divergence between the ZFC and FC curves at T_c is negligible, but it becomes prominent at approximately 200 K, suggesting a possible formation of magnetic domains, or the like in the measurement process. We would like to note that the range of the high-temperature part ($>T_c$) of the $\chi(T)$ curve is too narrow for a meaningful Curie–Weiss analysis (see the right side of Fig. 4).

The ac $\chi(=\chi' + i\chi'')$ of Ca_2MnOsO_6 was measured at temperatures between 5 and 320 K, and the χ' and χ" vs T curves are shown in Fig. 5. A sharp peak is observed at

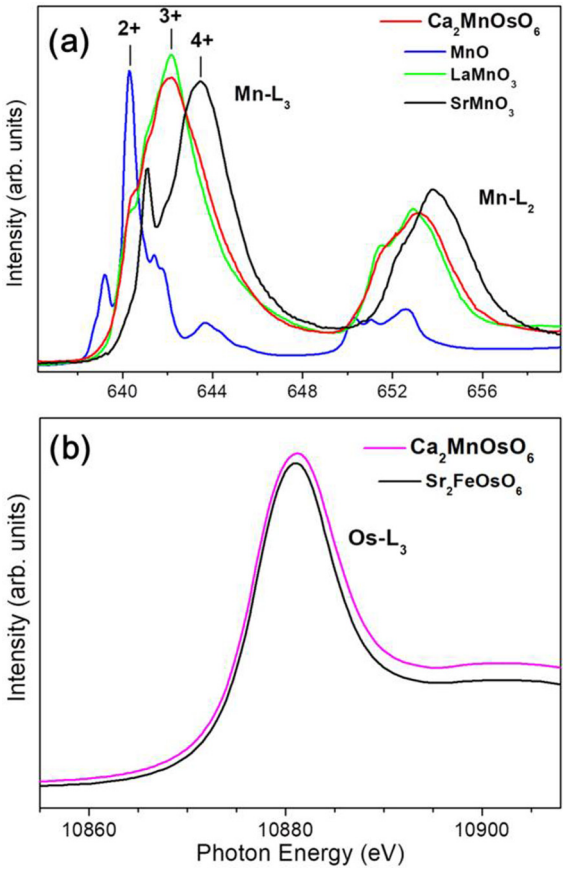

FIG. 2. (a) Room temperature Mn-$L_{2,3}$ XAS spectra of Ca_2MnOsO_6 and of MnO [44], $LaMnO_3$ [44], $SrMnO_3$ [45] as reference compounds for Mn^{2+}, Mn^{3+}, and Mn^{4+} valence states. (b) Os-L_3 XAS spectra of Ca_2MnOsO_6 and of Sr_2FeOsO_6 [46] as an Os^{5+} reference.

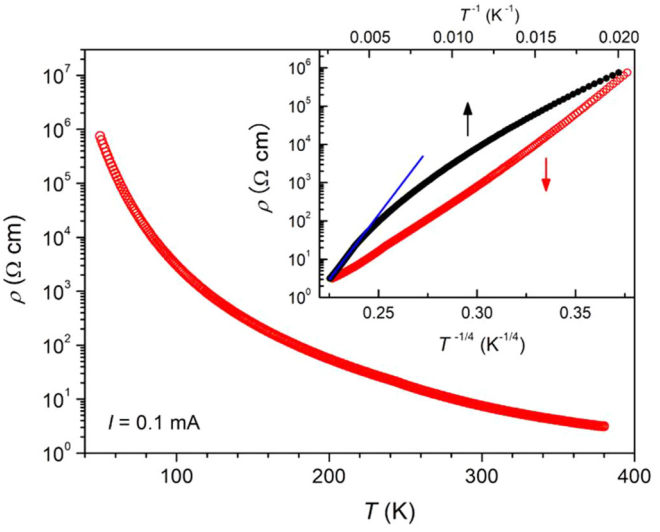

FIG. 3. Temperature dependence of ρ for polycrystalline Ca_2MnOsO_6. The inset shows an alternative plot of the data. The blue line indicates a fitting to the Arrhenius law at high temperatures (>300 K).

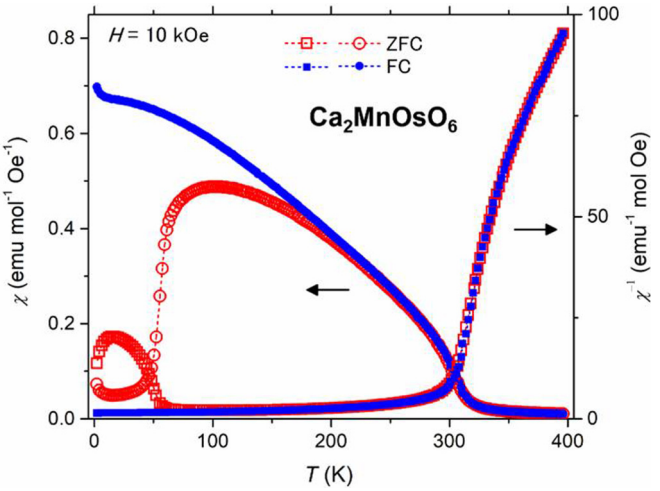

FIG. 4. Temperature dependence of χ of polycrystalline Ca_2MnOsO_6 measured in a field of 10 kOe. An alternative plot (T vs χ^{-1}) is shown on the right side.

305 K, which is consistent with the onset temperature of the $\chi(T)$ measurement. In contrast to multiple transitions found for Ca_2MnRuO_6, no additional anomaly is detected, indicating a single magnetic transition over the temperature range. Moreover, it substantiates that the divergence between the ZFC and FC curves in the $\chi(T)$ measurements is not caused by a magnetic transition. In Fig. 6, the temperature dependence of the heat capacity C_p shows an anomaly evolving at 305 K in zero magnetic field, and it becomes broader when a magnetic field of 70 kOe is applied. This observation supports that this anomaly is caused by a magnetic transition.

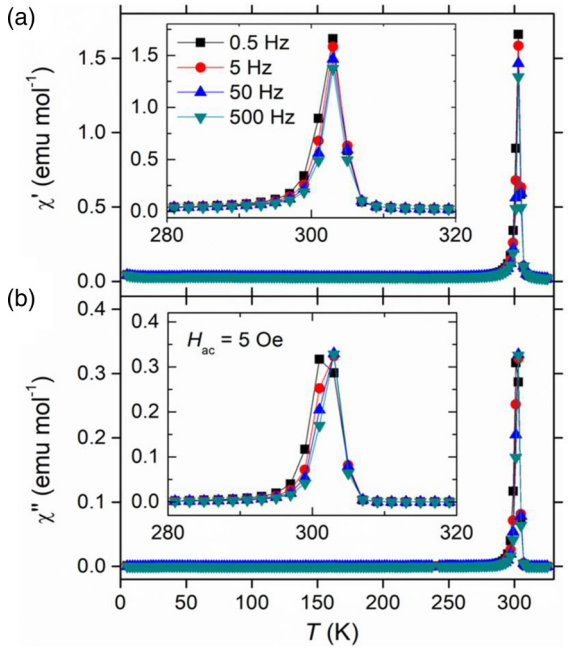

FIG. 5. (a) Real and (b) imaginary components of ac-magnetic susceptibility for polycrystalline Ca_2MnOsO_6 measured in an ac-magnetic field (H_{ac}) of 5 Oe at various frequencies. The inset shows a horizontal expansion around the magnetic transition temperature.

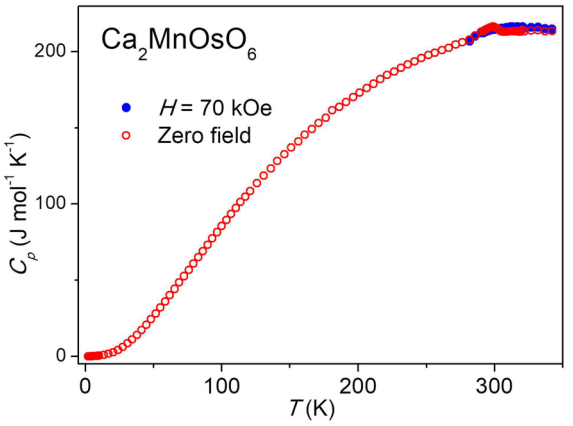

FIG. 6. Temperature dependence of specific heat capacity of Ca_2MnOsO_6.

The field dependence of the magnetization was measured at several temperatures between 2 and 350 K (see Fig. 7). The linear feature at 350 K confirms the paramagnetic behavior above T_c. In contrast, magnetic hysteresis appears at temperatures below T_c, suggesting that a FM component is involved in the magnetically ordered state. The magnetization at 2 K and 50 kOe is $1.40\,\mu_B$/f.u., which indicates the partial cancellation of the Mn and Os magnetic moments. The separate Mn and Os contributions to the total magnetic moment will be disentangled using the element specificity of XMCD (*vide infra*).

E. X-ray magnetic circular dichroism

Figure 8(a) shows the Mn-$L_{2,3}$ XAS spectrum (green) and the XMCD spectrum (blue), which is the difference between circularly polarized light with positive and negative helicities in an applied magnetic field of 60 kOe at 20 K. The XMCD signal can be clearly seen in Fig. 8(a). In order to extract the Mn moment, we performed the well-established configuration-interaction cluster calculations using the XTLS code [49]. The method uses a MnO_6 cluster, which includes explicitly the full atomic multiplet interaction, the

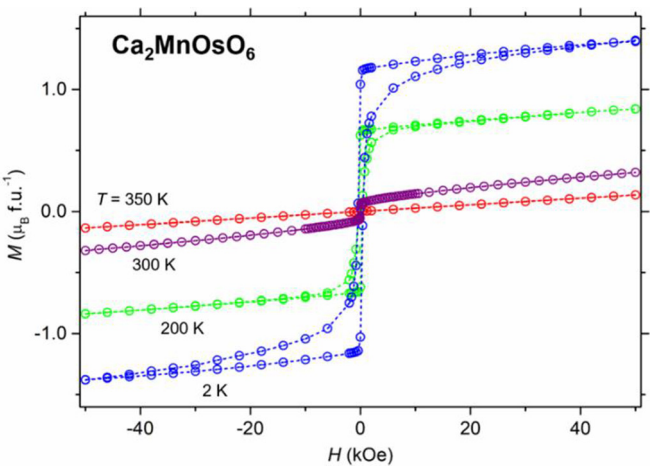

FIG. 7. Isothermal magnetization of polycrystalline Ca_2MnOsO_6 measured at various temperatures.

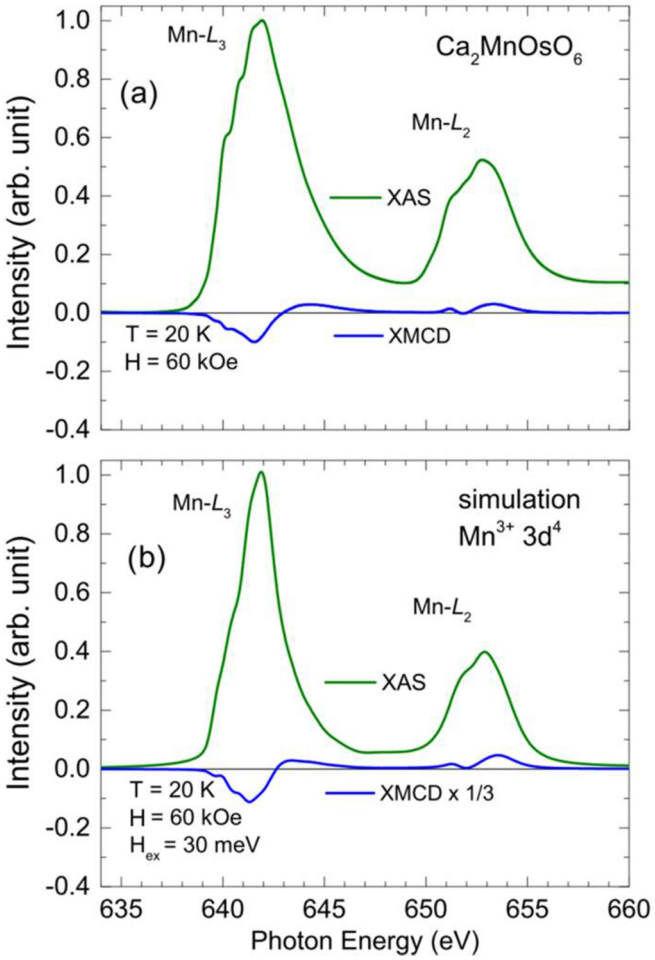

FIG. 8. (a) Mn-$L_{2,3}$ XAS (green) and XMCD (blue) spectra of Ca_2MnOsO_6 measured at 20 K under a magnetic field of 60 kOe and (b) the calculated XAS (green) and XMCD (blue) rescaled by a factor 1/3.

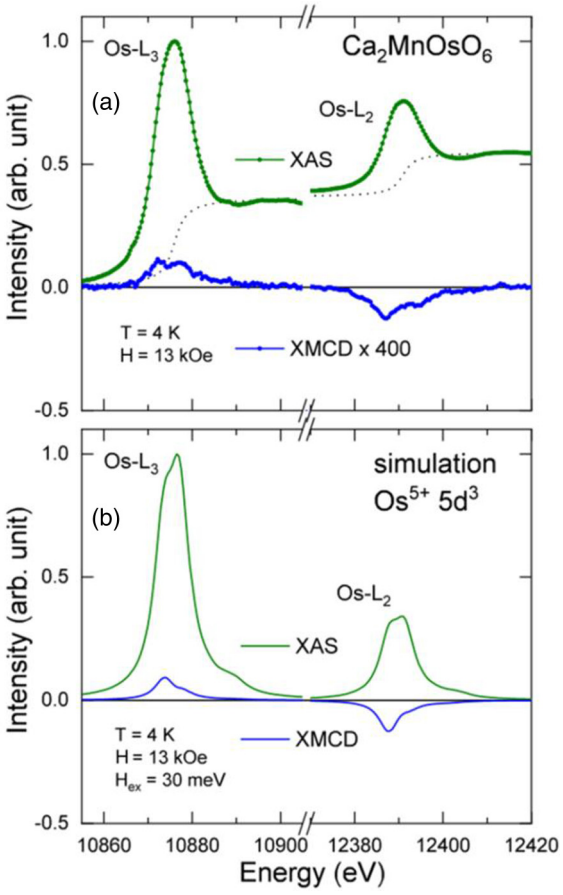

FIG. 9. (a) Os-$L_{2,3}$ XAS (green) and XMCD (blue multiplied by 400) spectra of Ca_2MnOsO_6 measured at 4 K under a magnetic field of 13 kOe. (b) the calculated Os-$L_{2,3}$ XAS (green) and XMCD (blue) spectra.

hybridization of the Mn with the oxygen ligands, and the crystal field acting on the Mn ions. The hybridization strengths and the crystal field parameters were taken from Ref. [50]. Figure 8(b) shows the calculated XAS (green) and XMCD (blue) for the Mn cluster in an exchange field (H_{ex}) of 30 meV. With this field (the energy scale of which reflects the experimentally determined T_c of 305 K) the Mn is fully magnetized having a moment of 3.9 μ_B. We observe that the line shape of the calculated XMCD spectrum is very similar to the experimental one, but we also notice that its magnitude is larger than measured. To reproduce the experimental size of XMCD signal in Fig. 8(a), we need to rescale the calculated XMCD spectrum by a factor of 1/3 as shown in Fig. 8(b). This implies that the XMCD experiment presents the net Mn moment of $3.9/3 = 1.3\,\mu_B$.

Figure 9 shows the Os-$L_{2,3}$ XAS spectrum (green curve) together with the XMCD spectrum (blue curve) measured below T_c in an applied magnetic field of 13 kOe at 4 K. The XMCD signal of the Os has an opposite sign as that of the Mn, which indicates an antiparallel alignment of Os magnetic moment with that of the Mn. We have also performed configuration-interaction cluster calculations using an OsO_6 cluster with parameters taken from Ref. [51]. Figure 9(b) shows the calculated XAS (green curve) and XMCD (blue curve) spectra. With an exchange field of 30 meV (T_c of 305 K) the Os is fully magnetized having a moment of 2.05 μ_B. The line shapes of the calculated spectra match very well those of the experiment. We notice, however, that the magnitude of the experimental XMCD is about 400 times smaller than that of the calculated, which suggests that most of the Os ions are magnetically disordered and/or antiferromagnetically aligned.

We would like to note that our finding from XMCD that the net Mn moment is 1.3 μ_B and that the net Os moment is very small (antiparallel aligned) is in excellent agreement with the magnetization measurement (see the previous section), which yielded a total net moment of 1.40 μ_B/f.u.

F. Density functional theory (DFT) calculation

We investigated the electronic and magnetic ground state of Ca_2MnOsO_6 by DFT calculations. In this theoretical study, we investigated a hypothetically ordered phase ($P2_1/n$; see Table S1, Figs. S1, and S2 in Supplemental Material [52]). The symmetry of the $P2_1/n$ structure has been reduced further to lower symmetry P-1 (space group: 2), which gives rise to two in-equivalent atoms each of Os and Mn, respectively.

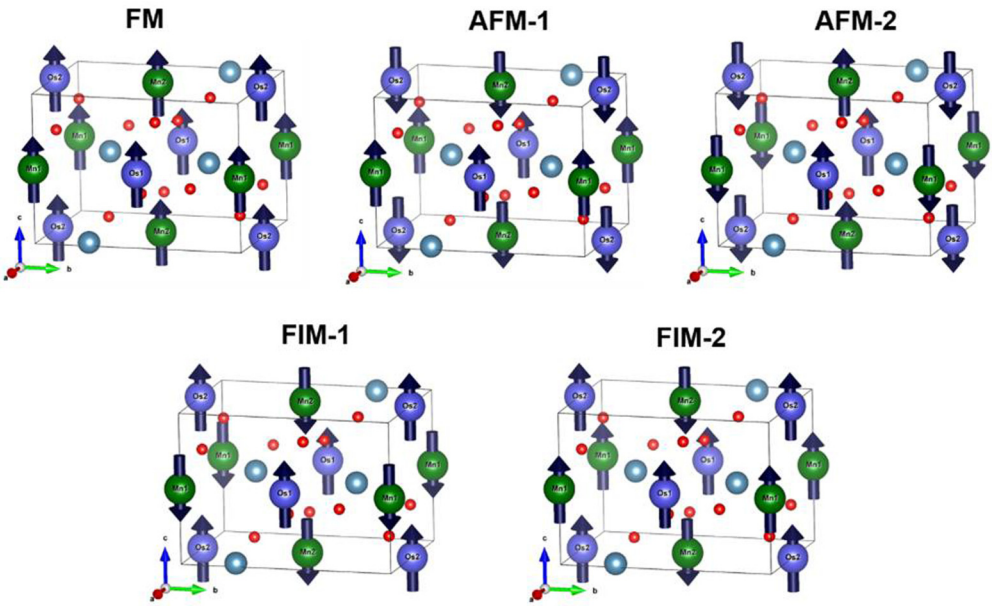

FIG. 10. Possible spin arrangements considered in the theoretical calculation for Ca_2MnOsO_6 with ordered Mn and Os atoms; ferromagnetic (FM), antiferromagnetic (AFM), and ferrimagnetic (FIM) configurations.

The magnetic ground state of the ordered phase was studied by calculating the total energy for each of the five different magnetic states, namely FM (FM-↑↑↑↑; Os1: Os2: Mn1: Mn2), two AFM (AFM-1-↑↓↑↓ and AFM-2-↑↓↓↑), and two FIM (FIM-1-↑↑↓↓ and FIM-2-↑↑↑↓) states (see Fig. 10). From the total energy calculations, FIM-1 is found to have the lowest energy, with an energy difference of 198 meV/unit cell to that of the next lowest order (AFM-1). The spin-polarized DFT calculations for the hypothetically ordered Ca_2MnOsO_6 suggest that the magnetic ground state is certainly FIM-1 with the antiparallel alignment of Mn moments to Os. The electronic ground state is HM (the HM gap is approximately 0.87 eV in the spin-up channel) within the GGA functional. Additionally, SOC effects has been considered where the spins are allowed to ordered along the [100] and [001] direction to check its influence on the electronic and related properties. Significant difference was not found for the net moments for Mn and Os (see Table III), while a reasonable change has been observed in the electronic behavior.

The electronic band structure and the spin-resolved density of states (DOS) (total and partial) within GGA functional are shown in Fig. 11 for the ordered phase, which is HM with an insulating band gap of ∼0.87 eV in the spin-up channel and metallic state in the spin-down channel. The major contributions to the total DOS around the E_F are attributed to the *Os*-5*d* orbitals in both spin channels, which hybridize strongly with the *O*-2*p* orbitals. From the partial DOS and band structure (see Fig. 11 and Fig. S3a [52]), the *Os*-5*d* orbitals in the spin-up channel are found to be fully occupied by $5d$-t_{2g} orbitals, which shows the Os^{5+} ($5d^3$) state. The six bands at and around the Fermi level ranging from −1.5 eV up to ∼ +0.7 eV are from the Os-$5d$-t_{2g} orbitals that hybridizes strongly with the *O*-2*p* orbitals (see Fig. 11 and Fig. S3a [52]) in spin-up and spin down channel. On the other hand, *Mn*-3*d* states are found to dominate mostly above +0.7 eV in the conduction region in spin-up channel, while in spin-down channel three *d* orbitals (d-t_{2g}) are fully occupied lying below −1.5 eV, while two of the *d* states (d-e_g) cross the Fermi level signaling the partial occupancy in spin-down channel. This feature is close to the ionic picture Mn^{3+} which should have four *d* states occupied. With SOC taken into account (within GGA), band splitting was observed (see Fig. S3a [52]), however, the overall band gap did not open. This suggests the necessity of using GGA+U.

To further investigate the experimentally observed semiconducting transport, we performed a GGA+*U* calculation

TABLE III. Spin $\langle m_s \rangle$ and orbital $\langle m_l \rangle$ moments measured by XMCD and two sets of theoretical values for ordered Ca_2MnOsO_6

	XMCD[a]		GGA+SO[b]			
			Ordered structure [100]		Ordered structure [001]	
	Mn	Os	Mn	Os	Mn	Os
$m_s(\mu_B/\text{atom})$	1.3	−0.005	3.13	−1.38	3.14	−1.41
$m_l(\mu_B/\text{atom})$	0.0	0.000	0.02	0.02	0.01	0.08
$m_s + m_l(\mu_B/\text{atom})$	1.3	−0.005	3.15	−1.36	3.16	−1.33

[a] $T = 4$ K and $H = 13$ kOe for Os and 20 K and 60 kOe for Mn.
[b] Standard generalized-gradient approximation with spin-orbit interaction.

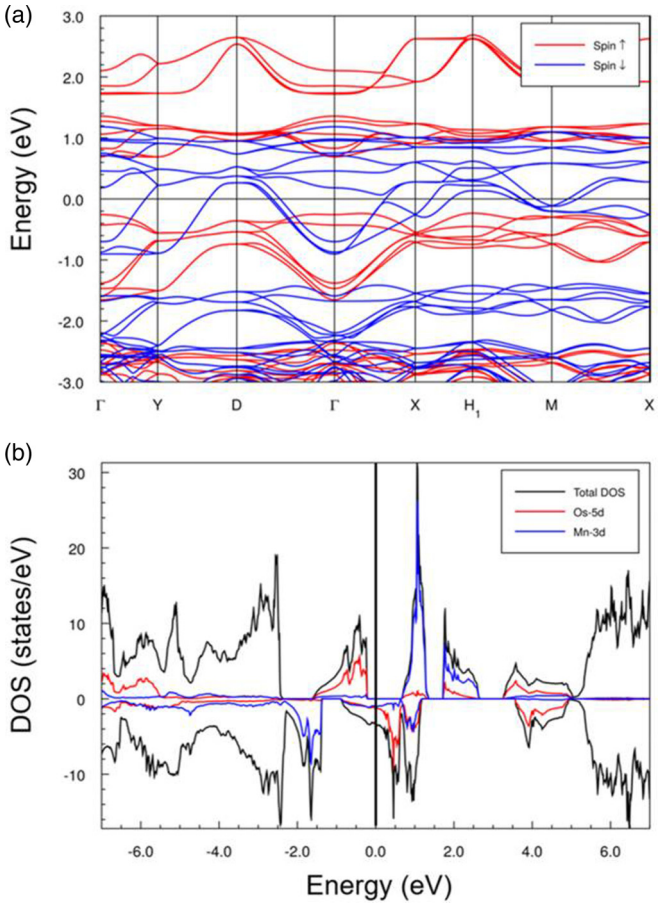

FIG. 11. (a) Band dispersion and (b) DOS of Ca_2MnOsO_6 with fully ordered Mn and Os atoms within GGA (optimized).

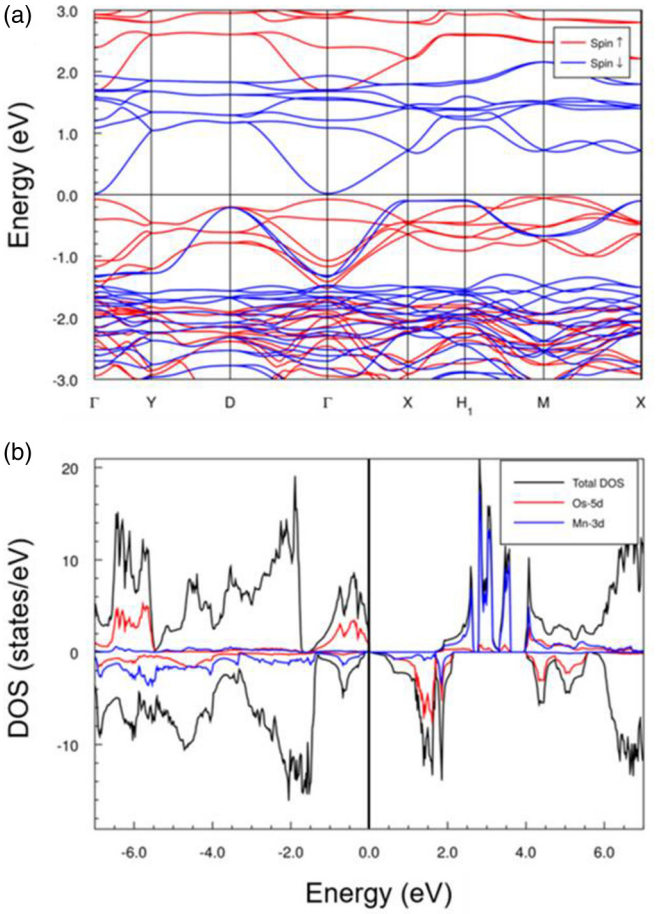

FIG. 12. (a) Band dispersion and (b) DOS of Ca_2MnOsO_6 with fully ordered Mn and Os atoms within GGA+U ($U = 5$ eV for Mn and 1.5 eV for Os atoms, respectively).

with U values ranging from 0–5 eV for Mn and 0–2.5 eV for Os [32–35]. The HM state changed to a semiconducting state at U(Mn) = 4 eV and U(Os) = 1.25 eV or higher [19]. With $U = 5$ eV for Mn and 1.5 eV for Os, the calculated DOS and band structure are shown in Fig. 12. A band gap of 0.11 eV was achieved, which agrees well with the experiment (∼0.11 eV). With SOC, an indirect band gap of 0.14 eV is found between the high symmetry point Γ and M, and a direct band gap of 0.21 eV at Γ point in the band dispersion shown in Fig. S3b [52]. Splitting of the orbitals for the easy axis [001] is large with a gap size of 0.14 eV. From the scalar relativistic DOS and band structure shown in Fig. 12, and relativistic fat bands in Fig. S3b [52], the *Os*-5*d* states are found to fully occupy with three t_{2g} orbitals in the spin-up channel and the remaining e_g orbitals are unoccupied, while in the spin-down channel, all the d bands lie above E_F. Most of the bands from *Mn*-3*d* around E_F hybridize with the *O*-2*p* and *Os*-5*d* states. The broad band lying just above E_F is mainly contributed by the *Mn*-3*d* orbital; the exchange energy splitting is of the order of ∼1.75 eV. Besides, MAE has been considered for the FIM-1 ground state. The calculated MAE is 29.6 meV/unit cell with its easy axis along the cubic [100] direction [53] within GGA. In contrast, within GGA+U, the easy axis is found along the out-of-plane with MAE of 3.46 meV/unit cell with all the spins aligned along the [001] direction.

To evaluate the impact from anti-site disorder on the electronic ground state, five different anti-site-disordered configurations (AS1, AS2, AS3, AS4, and AS5) were created as shown in the Fig. S4 [52], where a $1 \times 1 \times 2$ supercell has been generated that corresponds to a total of 40 atoms in a unit cell. DFT calculations were first carried out on these five different anti-site-disorder cases with FIM spin state. However, in comparison with the ordered FIM-1 case these anti-site-disordered cases showed higher energies within ∼0.6 to 1.37 meV/unit-cell (see Table S2 [52]), with energies that AS1 < AS2 < AS3 < AS4 < AS5. We further calculated these anti-site-disordered cases with FM spin state. Energy differences (ΔE) between FM and FIM states in the respective anti-site-disordered cases are summarized in Table S3 [52]. FIM states showed lower energies, indicating that AFM alignment is favorable between Mn-Os, while FM coupling may be favorable among the Mn-Mn or Os-Os, giving rise to long-range FIM order in the anti-site-disordered Ca_2MnOsO_6. The electronic band gap is noted for AS1 and AS2 cases, while others remain metallic within GGA+U (see Table S2 [52]).

IV. DISCUSSION

We synthesized an anti-site-disordered double perovskite Ca_2MnOsO_6 (equivalent to $CaMn_{0.5}Os_{0.5}O_3$) with Mn^{3+} and

Os^{5+} ions randomly distributed at the B site of the perovskite. It is noteworthy that neighbor compounds Ca_2FeOsO_6 and Ca_2CrOsO_6 all crystallize in ordered double perovskite structure with rocksalt arrangement of FeO_6/CrO_6 and OsO_6 octahedra. The B and B' site ordering in double perovskite is generally determined by the charge difference and effective ionic size difference of B and B' ions [54]. Given that Mn^{3+} has the same effective ionic radii (0.645 Å) as that of Fe^{3+} in octahedral coordination [55], the reason for the absence of Mn^{3+} and Os^{5+} ordering in Ca_2MnOsO_6 is unclear, although perhaps the JT distortions induced around the Mn^{3+} ions may play an important role. Despite the absence of Mn^{3+} and Os^{5+} ordering, Ca_2MnOsO_6 is electrically semiconducting and features a remarkably high T_c above room-temperature (305 K).

To rationalize the magnetic properties, we first consider the double perovskite Ca_2MnOsO_6 with perfect Mn^{3+} and Os^{5+} ordering. Our band structure calculations suggest that this would lead to a FIM ground state, where the moments of Mn^{3+} ($t_{2g}^3 e_g^1$) and Os^{5+} (t_{2g}^3) are arranged antiparallel. In order to interpret this result, we notice that the nearest-neighbor $Mn^{3+}-O-Os^{5+}$ super-exchange coupling can either be FM (the Mn^{3+} e_g electrons hop on to the empty Os^{5+} e_g states) or AFM (the down spin Os^{5+} t_{2g} electrons hop on to the Mn^{3+} t_{2g} states). In comparison to $3d$ ions, the $5d$ ions have much enhanced crystal field splitting, therefore the FM coupling involving the virtual hopping between e_g orbitals becomes weak. In particular when the crystal structure is distorted this FM coupling can become even weaker [47,56], with the result that the AFM $Mn^{3+}-O-Os^{5+}$ coupling is the dominant interaction and generate the FIM state in the hypothetically ordered Ca_2MnOsO_6.

Introducing now anti-site disorder in Ca_2MnOsO_6, we will have also NN $Os^{5+}-O-Os^{5+}$ and $Mn^{3+}-O-Mn^{3+}$ interactions. The $Os^{5+}-O-Os^{5+}$ coupling is AFM as shown in AFM $NaOsO_3$ [43,57]. The Os^{5+} moments are therefore expected to compensate each other in such a situation. This would then be consistent with the experimental observation that the Os XMCD effect is very small. The case concerning the $Mn^{3+}-O-Mn^{3+}$ interactions is more complex. Depending on the orbital orientation due to the JT distortion of Mn^{3+}, the interaction can be either FM or AFM which has been well discussed in $LaMnO_3$ [42,58–61]. In our crystal structure analysis, the contribution from the JT effect of Mn^{3+} was clearly noticed (see crystal structure part). The moment, 1.3 μ_B/Mn^{3+}, obtained from Mn XMCD is not negligible, but smaller than the theoretically calculated 3.15 μ_B/Mn^{3+} for ordered Ca_2MnOsO_6 phase (see Table III) and also smaller than the 3.9 μ_B/Mn^{3+} from the cluster calculations. This indicates that there are competing FM and AFM $Mn^{3+}-O-Mn^{3+}$ interactions. Studies of highly anti-site-disordered double perovskite $A_2Mn^{3+}B'O_6$ (A = Ca, Sr; B' = Ta, Sb), in which only Mn^{3+} is magnetic, found that the FM interactions are dominant in these compounds with positive Weiss temperatures varied from 64–107 K [62]. A large FM component with a magnetization of about 1.47 μ_B/Mn^{3+} (at 5 K and 50 kOe) was observed in Sr_2MnTaO_6 despite its glassy state at low temperatures [62]. These results are thus similar to our Ca_2MnOsO_6 case.

Recent theoretical and experimental studies of the anti-site disorder on the magnetic properties of Sr_2FeMoO_6, Sr_2FeReO_6, Sr_2CrReO_6, Sr_2CrOsO_6, and Sr_2FeRuO_6 suggested that the anti-site disorder suppresses T_c or destroys the magnetically ordered state, because the anti-site disorder introduces strong AFM $Fe^{3+}-O-Fe^{3+}$ and $Cr^{3+}-O-Cr^{3+}$ interactions to hinder the long-range magnetic order [11–14,63–65]. Different from Fe^{3+} and Cr^{3+}, the $Mn^{3+}-O-Mn^{3+}$ superexchange interactions can be both FM and AFM [42,58–61] depending on the orbital orientation, which may help to maintain net partial Mn^{3+} moments and also a high T_c in this anti-site-disordered Ca_2MnOsO_6. This scenario is likely to be different from the ferrimagnetism of anti-site-disordered Ca_2MnRuO_6 [17,18], where the presence of mixed valence states of $Mn^{3+}/Mn^{4+}-Ru^{4+}/Ru^{5+}$ would also lead to a ferromagnetic double exchange mechanism for the $Mn^{3+}-Mn^{4+}$ and a HM state for Ca_2MnRuO_6 [17–19].

V. CONCLUSION

Anti-site-disordered Ca_2MnOsO_6 was synthesized under high-pressure (6 GPa). It crystallizes into an orthorhombic structure (space group: *Pnma*), in which trivalent Mn and pentavalent Os share the Wycoff $4b$ position without an ordered arrangement. Ca_2MnOsO_6 is electrically semiconducting. XAS measurement confirmed the trivalent Mn and pentavalent Os oxidation states. The XMCD reveals the antiparallel alignment of the net Mn and Os magnetic moments. Remarkable is that the net Mn moment is only about 1/3 of its full Mn^{3+} value and that the net Os moment is very small. We have discussed the strength and sign of various intersite exchange interactions in this material using data from band structure calculations, taking into account also the presence of anti-site disorder and JT distortions around the Mn^{3+} ions. The T_c = 305 K is the second highest in the material category of so-called disordered ferromagnets and could therefore be useful in the development of oxide spintronic devices that are less sensitive for anti-site disorder during fabrication.

ACKNOWLEDGMENTS

M.P.G. thanks the Alexander von Humboldt Foundation for the financial support through HERMES program and U. Nitzsche for the technical support. This study was supported in part by JSPS KAKENHI Grant No. JP16H04501, a research grant from Nippon Sheet Glass Foundation for Materials and Engineering (#40-37), and Innovative Science and Technology Initiative for Security, ATLA, Japan. We acknowledge support from the Max Planck-POSTECH-Hsinchu Center for Complex Phase Materials. The work in Dresden was partially supported by the Deutsche Forschungsgemeinschaft through SFB 1143 (Project-id 247310070). The synchrotron radiation experiments were performed at the NIMS synchrotron x-ray station at SPring-8 with the approval of the Japan Synchrotron Radiation Research Institute (Proposals No. 2017A4503, No. 2017B4502, No. 2018A4501, and No. 2018B4502). M.G. acknowledges the support of Grant No. NSF-DMR-1507252 from the United States.

[1] K. I. Kobayashi, T. Kimura, H. Sawada, K. Terakura, and Y. Tokura, Nature (London) **395**, 677 (1998).

[2] R. Morrow, J. R. Soliz, A. J. Hauser, J. L. Gallagher, M. A. Susner, M. D. Sumption, A. A. Aczel, and J. Yan *et al.*, J. Solid State Chem. **238**, 46 (2016).

[3] Y. Krockenberger, K. Mogare, M. Reehuis, M. Tovar, M. Jansen, G. Vaitheeswaran, V. Kanchana, F. Bultmark, and A. Delin *et al.*, Phys. Rev. B **75**, 020404(R) (2007).

[4] J. Longo and R. Ward, J. Am. Chem. Soc. **83**, 2816 (1961).

[5] K. I. Kobayashi, T. Kimura, Y. Tomioka, H. Sawada, K. Terakura, and Y. Tokura, Phys. Rev. B **59**, 11159 (1999).

[6] F. K. Patterson, C. W. Moeller, and R. Ward, Inorg. Chem. **2**, 196 (1963).

[7] H. L. Feng, M. Arai, Y. Matsushita, Y. Tsujimoto, Y. Guo, C.I. Sathish, X. Wang, Y.-H. Yuan, and M. Tanaka *et al.*, J. Am. Chem. Soc. **136**, 3326 (2014).

[8] R. Morrow, J. W. Freeland, and P. M. Woodward, Inorg. Chem. **53**, 7983 (2014).

[9] H.L. Feng, S. Calder, M.P. Ghimire, Y.-H. Yuan, Y. Shirako, Y. Tsujimoto, Y. Matsushita, Z. Hu, C.-Y. Kuo, and L.H. Tjeng *et al.*, Phys. Rev. B **94**, 235158 (2016).

[10] H. L. Feng, P. Adler, M. Reehuis, W. Schnelle, P. Pattison, A. Hoser, C. Felser, and M. Jansen, Chem. Mater. **29**, 886 (2017).

[11] A. J. Hauser, R. E. A. Williams, R. A. Ricciardo, A. Genc, M. Dixit, J. M. Lucy, P. M. Woodward, H. L. Fraser, and F. Yang, Phys. Rev. B **83**, 014407 (2011).

[12] J. Navarro, J. Nogués, J. S. Muñoz, and J. Fontcuberta, Phys. Rev. B **67**, 174416 (2003).

[13] C. Meneghini, S. Ray, F. Liscio, F. Bardelli, S. Mobilio, and D. D. Sarma, Phys. Rev. Lett. **103**, 046403 (2009).

[14] Y. H. Huang, M. Karppinen, H. Yamauchi, and J. B. Goodenough, Phys. Rev. B **73**, 104408 (2006).

[15] T. He and R. J. Cava, J. Phys.: Condens. Matter **13**, 8347 (2001).

[16] G. Cao, F. Freibert, and J. E. Crow, J. Appl. Phys. **81**, 3884 (1997).

[17] R. A. Ricciardo, H. L. Cuthbert, P. M. Woodward, Q. Zhou, B. J. Kennedy, Z. Zhang, M. Avdeev, and L.-Y. Jang, Chem. Mater. **22**, 3369 (2010).

[18] T. Taniguchi, S. Mizusaki, N. Okada, Y. Nagata, S. H. Lai, M. D. Lan, N. Hiraoka, M. Itou, and Y. Sakurai *et al.*, Phys. Rev. B **77**, 014406 (2008).

[19] R. Mishra, J. R. Soliz, P. M. Woodward, and W. Windl, Chem. Mater. **24**, 2757 (2012).

[20] A. J. Williams, A. Gillies, J. P. Attfield, G. Heymann, H. Huppertz, M. J. Martínez-Lope, and J. A. Alonso, Phys. Rev. B **73**, 104409 (2006).

[21] K. Yamaura, J. Solid State Chem. **236**, 45 (2016).

[22] M. Tanaka, Y. Katsuya, Y. Matsushita, and O. Sakata, J. Ceram. Soc. Jpn. **121**, 287 (2013).

[23] M. Tanaka, Y. Katsuya, and A. Yamamoto, Rev. Sci. Instrum. **79**, 075106 (2008).

[24] K. Momma and F. Izumi, J. Appl. Crystallogr **44**, 1272 (2011).

[25] F. Izumi and T. Ikeda, Mater. Sci. Forum **321–324**, 198 (2000).

[26] B. L. Henke, E. M. Gullikson, and J. C. Davis, At. Data Nucl. Data Tables **54**, 181 (1993).

[27] K. Koepernik and H. Eschrig, Phys. Rev. B **59**, 1743 (1999).

[28] J. P. Perdew, K. Burke, and M. Ernzerhof, Phys. Rev. Lett. **77**, 3865 (1996).

[29] P. Blaha, K. Schwarz, G. K. H. Madsen, D. Kvasnicka, and J. Luitz, *WIEN2K, An Augmented Plane Wave + Local Orbitals Program for Calculating Crystal Properties* (Karlheinz Schwarz, Techn. Universität Wien, Austria, 2001).

[30] V. I. Anisimov, I. V. Solovyev, M. A. Korotin, M. T. Czyzyk, and G. A. Sawatzky, Phys. Rev. B **48**, 16929 (1993).

[31] E. R. Ylvisaker, W. E. Pickett, and K. Koepernik, Phys. Rev. B **79**, 035103 (2009).

[32] M. P. Ghimire, L.-H. Wu, and X. Hu, Phys. Rev. B **93**, 134421 (2016).

[33] Y. Yuan, H. L. Feng, M. P. Ghimire, Y. Matsushita, Y. Tsujimoto, J. He, M. Tanaka, Y. Katsuya, and K. Yamaura, Inorg. Chem. **54**, 3422 (2015).

[34] H. Wang, S. Zhu, X. Ou, and H. Wu, Phys. Rev. B **90**, 054406 (2014).

[35] B. J. Kim, H. Jin, S. J. Moon, J. Y. Kim, B. G. Park, C. S. Leem, J. Yu, T. W. Noh, and C. Kim *et al.*, Phys. Rev. Lett. **101**, 076402 (2008).

[36] M. P. Ghimire and X. Hu, Mater. Res. Express **3**, 106107 (2016).

[37] G. King and P. M. Woodward, J. Mater. Chem. **20**, 5785 (2010).

[38] G. King, A. M. Abakumov, P. M. Woodward, A. Llobet, A. A. Tsirlin, D. Batuk, and E. V. Antipov, Inorg. Chem. **50**, 7792 (2011).

[39] H. Kato, T. Okuda, Y. Okimoto, Y. Tomioka, K. Oikawa, T. Kamiyama, and Y. Tokura, Phys. Rev. B **69**, 184412 (2004).

[40] Y. Shi, Y. Guo, Y. Shirako, W. Yi, X. Wang, A. A. Belik, Y. Matsushita, H.L. Feng, and Y. Tsujimoto *et al.*, J. Am. Chem. Soc. **135**, 16507 (2013).

[41] K. R. Poeppelmeier, M. E. Leonowicz, J. C. Scanlon, J. M. Longo, and W. B. Yelon, J. Solid State Chem. **45**, 71 (1982).

[42] J. Rodríguez-Carvajal, M. Hennion, F. Moussa, A. H. Moudden, L. Pinsard, and A. Revcolevschi, Phys. Rev. B **57**, R3189 (1998).

[43] Y. G. Shi, Y. F. Guo, S. Yu, M. Arai, A. A. Belik, A. Sato, K. Yamaura, E. Takayama-Muromachi, and H. F. Tian *et al.*, Phys. Rev. B **80**, 161104(R) (2009).

[44] C. Mitra, Z. Hu, P. Raychaudhuri, S. Wirth, S. I. Csiszar, H. H. Hsieh, H. J. Lin, C. T. Chen, and L. H. Tjeng, Phys. Rev. B **67**, 092404 (2003).

[45] A. N. Vasiliev, O. S. Volkova, L. S. Lobanovskii, I. O. Troyanchuk, Z. Hu, L. H. Tjeng, D. I. Khomskii, H. J. Lin, and C. T. Chen *et al.*, Phys. Rev. B **77**, 104442 (2008).

[46] H. L. Feng, M. Reehuis, P. Adler, Z. W. Hu, M. Nicklas, A. Hoser, S. C. Weng, C. Felser, and M. Jansen, Phys. Rev. B **97**, 184407 (2018).

[47] L. S. I. Veiga, G. Fabbris, M. van Veenendaal, N. M. Souza-Neto, H. L. Feng, K. Yamaura, and D. Haskel, Phys. Rev. B **91**, 235135 (2015).

[48] P. W. Anderson, Phys. Rev. **109**, 1492 (1958).

[49] A. Tanaka and T. Jo, J. Phys. Soc. Jpn. **63**, 2788 (1994).

[50] J. M. Chen, Z. Hu, H. T. Jeng, Y. Y. Chin, J. M. Lee, S. W. Huang, K. T. Lu, C. K. Chen, S. C. Haw, and T. L. Chou *et al.*, Phys. Rev. B **81**, 201102(R) (2010).

[51] OsO_6 cluster parameters [eV]: Udd = 1.0, Upd = 2.0, ionic crystal field 10Dq = 2.3, charge transfer energy $\Delta_{CT} = -1.5$, hybridization $V(e_g) = 5.15$, $V(t_{2g}) = 2.89$, ligand-crystal field $10Dq_{li_g} = 0.93$, spin orbit coupling $\zeta_{5d} = 0.4$, exchange field $H_{ex} = 0.030$, and magnetic field 13 kOe. The Slater integrals were reduced to 70% of Hartree-Fock values. For all simulations we have considered the thermal population of the different states using a Boltzmann distribution.

[52] See Supplemental Material at http://link.aps.org/supplemental/10.1103/PhysRevMaterials.3.124404 for the ordered and disordered structures used for DFT calculations,and parts of DFT calculated results.

[53] A. A. J. Zeisner, S. Selter, S. Aswartham, M. P. Ghimire, M. Richter, J. van den Brink, B. Büchner, and V. Kataev, Phys. Rev. B **99**, 165109 (2019).

[54] M. T. Anderson, K. B. Greenwood, G. A. Taylor, and K. R. Poeppelmeier, Prog. Solid State Chem. **22**, 197 (1993).

[55] R. D. Shannon, Acta Crystallogr. A **32**, 751 (1976).

[56] Y. S. Hou, H. J. Xiang, and X. G. Gong, Sci. Rep. **5**, 13159 (2015).

[57] S. Calder, V. O. Garlea, D. F. McMorrow, M. D. Lumsden, M. B. Stone, J. C. Lang, J. W. Kim, J. A. Schlueter, and Y. G. Shi *et al.*, Phys. Rev. Lett. **108**, 257209 (2012).

[58] Y. Murakami, J. P. Hill, D. Gibbs, M. Blume, I. Koyama, M. Tanaka, H. Kawata, T. Arima, and Y. Tokura *et al.*, Phys. Rev. Lett. **81**, 582 (1998).

[59] I. Solovyev, N. Hamada, and K. Terakura, Phys. Rev. Lett. **76**, 4825 (1996).

[60] L. F. Feiner and A. M. Oles, Phys. Rev. B **59**, 3295 (1999).

[61] T. Mizokawa, D. I. Khomskii, and G. A. Sawatzky, Phys. Rev. B **60**, 7309 (1999).

[62] T. K. Mandal, V. V. Poltavets, M. Croft, and M. Greenblatt, J. Solid State Chem. **181**, 2325 (2008).

[63] A. Halder, P. Sanyal, and T. Saha-Dasgupta, Phys. Rev. B **99**, 020402(R) (2019).

[64] J. Chang, K. Lee, M. H. Jung, J.-H. Kwon, M. Kim, and S.-K. Kim, Chem. Mater. **23**, 2693 (2011).

[65] P. D. Battle, T. C. Gibb, C. W. Jones, and F. Studer, J. Solid State Chem. **78**, 281 (1989).